

# Simulated Response of MuTe, a Hybrid Muon Telescope

A. Vásquez-Ramírez,<sup>1,\*</sup> M. Suárez-Durán,<sup>2</sup> A. Jaimes-Motta,<sup>1</sup> R. Calderón-Ardila,<sup>3,4</sup> J. Peña-Rodríguez,<sup>1</sup> J. Sánchez-Villafrades,<sup>5</sup> J.D. Sanabria-Gómez,<sup>1</sup> H. Asorey,<sup>3,6,7</sup> and L.A. Núñez<sup>1,8</sup>

<sup>1</sup>*Escuela de Física, Universidad Industrial de Santander, Bucaramanga, Colombia*

<sup>2</sup>*Departamento de Física y Geología, Universidad de Pamplona, Pamplona, Colombia*

<sup>3</sup>*Instituto de Tecnologías en Detección y Astropartículas, Centro Atómico Constituyentes, Comisión Nacional de Energía Atómica, Buenos Aires, Argentina*

<sup>4</sup>*Universidad Nacional de San Martín, Instituto SABATO, Argentina*

<sup>5</sup>*Escuela de Ingeniería Eléctrica, Electrónica y de Telecomunicaciones, Universidad Industrial de Santander, Bucaramanga, Colombia*

<sup>6</sup>*Centro Atómico Bariloche, Comisión Nacional de Energía Atómica, San Carlos de Bariloche, Argentina*

<sup>7</sup>*Escuela de Producción, Tecnología y Medio Ambiente, Universidad Nacional de Río Negro, San Carlos de Bariloche, Argentina*

<sup>8</sup>*Departamento de Física, Universidad de Los Andes, Mérida, Venezuela*

In this paper we present a complete and detailed computational model of the hybrid response of the Muon Telescope (MuTe), designed to perform muography volcanic studies. This instrument combines two particle detection techniques: first, a muon hodoscope based on two planes of plastic scintillator bars; and a Water Cherenkov detector located behind the rear scintillator panel acting as a third coincidence and discriminating detector.

The simulation model includes materials, geometries, dimensions, and the photo-sensitive devices of the detectors, and the detectors response to the expected muon flux at 2650 m a.s.l at Cerro Machín Volcano, Colombia. The obtained results, in agreement with several experimental setups, were used to set up the detector trigger for muon detection in terms of the expected signal for a muon depositing energy at each component of the instrument.

Keywords: Muography, Volcanic Risk, Detector simulations, Water Cherenkov Detectors,

## I. INTRODUCTION

Cosmic rays (CR) are continuously impinging the Earth's atmosphere producing cascades of secondary particles called extensive air showers (EAS), having three main components: the electromagnetic, the hadronic, and the muonic. The electromagnetic component produced by electrons, positrons, and photons, coupled through several processes. The hadronic component generated by baryons and mesons produced through QCD interactions, and the muonic component, caused mainly of muons coming from the decay of charged pions, kaons, and other charged mesons through weak interactions processes. The energy of these muons comprises a broad spectrum, but only those muons with the highest energies ( $> 1\text{TeV}$ ) – produced during the very first interactions of the evolving particles cascade – such as the decay of charmed mesons, are collectively known as prompt muons and have enough energy to cross from hundreds to thousand meters of rock [1].

Muography is an emerging technique based on measuring the attenuation of the directional muon flux moving across geological or anthropic structures [2]. Nowadays we are witnessing several new successful academic and commercial applications such as the detection of hidden materials in containers [3], archaeological building scanning [4, 5], nuclear plant inspection [6], nuclear waste monitoring, underground cavities [7], the overburden of railway tunnels [8] and vulcanology applications (see, e.g., [9] and references therein).

The existence of more than a dozen active volcanoes in Colombia, which represents significant risks to the nearby population [10–12], motivates local research groups to explore possible applications of the muography technique [13–18].

Hodoscopes are the most common detectors designed and implemented for volcano muography. They consist of two or more panels devised to identify muon trajectories. Projects like MU-RAY [19], ToMuVol [20], and DIAPHANE [21] use hodoscopes based on different detection technologies: emulsion plates, resistive plate chambers, micromegas, multi-wire proportional cameras, and scintillators, just to mention the most common ones. Each of these techniques has advantages and disadvantages: Emulsion plate detectors [4, 22] provide an excellent spatial resolution of the order of sub-microns, are passive, and easy to handle. On the other side, they have short lifetimes, and it is not possible to discriminate the time-stamp of dynamic phenomena, because the recorded events accumulate in the plates. Gas detectors, as Resistive Plate Chambers [23, 24], Micromegas [25], and Multi-Wire Proportional Cameras [26], allow obtaining short traces of the detected particles with a spatial resolution around the microns. However, for such a low muon flux, it is difficult to address the benefits of this high spatial resolution fully and, since these detectors operate outdoors, environmental temperature variability could affect the detector operation. Finally, scintillation based detectors, using segmented [6, 27, 28] or continuous scintillators [29–31] – which does not present a considerable mechanical variation caused by environmental conditions – are more robust and more affordable than gaseous and emulsion detectors. Nevertheless, their spatial resolution

\* Corresponding author: Carrera 27 calle 9 Ciudad Universitaria. Bucaramanga, Colombia., adrianacvr67@gmail.com

is not as good as the other detectors since the segments generally used are of the order of centimeters.

In this paper, we present a detailed computational *Geant4* model of our hybrid Muon Telescope (*MuTe*) and the estimation of its response for an expected atmospheric muon flux at 2650 m a.s.l at Cerro Machín Volcano-Colombia. *MuTe* combines two detection techniques: a hodoscope with two detection planes of plastic scintillator bars, and a Water Cherenkov Detector (*WCD*) which acts as an absorbing element and as a third active coincidence detector. The model includes materials, detailed geometries and dimensions, and the detector's photo-sensitive devices. In the next section, we briefly describe the rationale behind the *MuTe* design. Section III discussed the response from scintillator bar hodoscope to the impinging cosmic ray background. We emphasize in the bar scintillator model and the possible attenuation effects. In section III B, we compare our simulation results with data emerging from an experimental laboratory setup and study the temperature effect on breakdown voltage for the silicon photomultiplier (*SiPM*) used in the scintillator panels. Section IV presents the response of the *WCD* and also compare some of the results with recent lab measurements. Finally in section V we summarize some final remarks and conclusions.

## II. THE MUTE INSTRUMENTAL DESIGN

As we have mentioned above, our Muon Telescope (sketched in figure 1) is a hybrid detector that combines two technologies: a two-panel scintillator bar hodoscope, and a water Cherenkov detector, increasing the signal/noise separation and the backward noise [32–35]. This hybrid technique allows us to estimate not only the incoming flux directions but also the range of deposited energy of the impinging particles [13, 18].

The panels of the hodoscope consist in an array of 30 vertical  $\times$  30 horizontal scintillator bars, of 4cm wide, 1cm thick and 120cm long, providing a total of 900 pixels of 4cm  $\times$  4cm, yielding a total detection surface of 14.400cm<sup>2</sup>. Scintillation bars are made of Styron<sup>TM</sup> 665-W polystyrene doped with a mixture of liquid organic scintillators: 1% of 2,5-diphenyloxazole (PPO) and 0.03% of 1,4-bis (5-phenyloxazol-2-yl) benzene (POPOP) [36], having a photon emission peak at the wavelength of 420nm. Each bar has a 0.25 mm highly reflective coat made of 85% Polystyrene and 15% of TiO<sub>2</sub>. At the center, each bar has a  $\sim$  3mm diameter hole longitudinally extruded, where is placed a 1 mm, wavelength shifter (WLS) and multi-cladded optical fiber Saint Gobain BCF92. The fiber core is made of Poly-methyl methacrylate, having the first clad of Polyethylene, and the external one of Fluorinated Polyethylene [37]. Scintillation photons produced by the passage of charged particles through the bars are partially collected by the fiber, absorbed, and re-emitted in a different wave and transported along the fiber. One of the extremes of the fiber is polished at an angle of 45 degrees to increase internal reflection and to favor photon collection in the opposite extreme. Mechanically coupled to the fiber, is a silicon photomultiplier Hama-

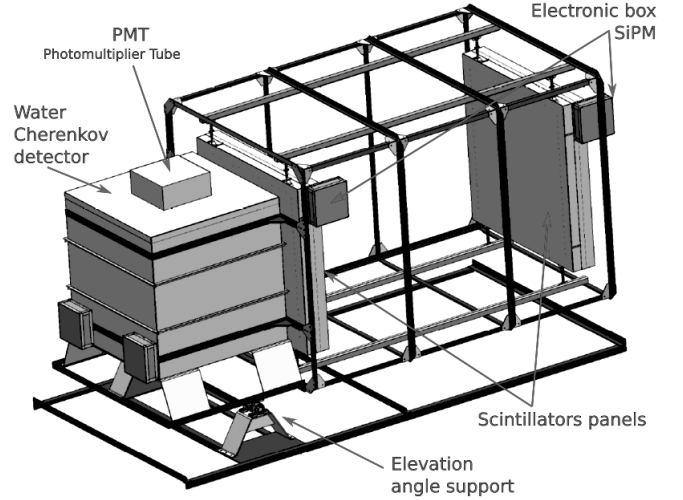


Fig. 1. A sketch of the hybrid detector *MuTe*: a two-panel scintillator bar hodoscope in front and a Water Cherenkov Detector (*WCD*) at the back. Each panel of the scintillator bar hodoscope has 900 detection pixels to determine the incoming directions of the particles. The *WCD* is a stainless steel container of 120cm side, coated inside with Tyvek, holding a *PMT* at the center of the roof to detect the Cherenkov radiation and devised to filter most of the backward & background noise of muography. The mechanical structure has a variable elevation angle to adjust the telescope according to the object under study, and it is possible to adjust scintillator panels separation to modify the pixel spatial resolution.

matsu S13360-1350CS, which has a photosensitive surface of 1.3 mm  $\times$  1.3 mm, consisting of 2668 avalanche photodiodes [38]. This device has a spectral detection range from 270 to 900nm, with its maximum sensitivity around 450nm.

Casual coincidences detection and discriminations of muons signals from background noise are enhanced by using our own developed Time-of-Flight (*ToF*) recording system, complemented by a cubic 120 cm side water Cherenkov detector (sketched in figure 1). The *WCD* consists of a cubic stainless steel water container, internally coated with a reflective and diffusive material 0.4 mm Tyvek [39] and filled with 1.7 m<sup>3</sup> of purified water, having an 8" Hamamatsu R5912 photomultiplier tube (*PMT*) placed at the center of the tank roof. In this way, the photosensitive *PMT* window is in direct contact with the water and can detect Cerenkov photons produced by relativistic charged particles moving through the detector (see figure 1).

This implemented desing filters the soft-component ( $e^\pm$ ) of Extensive Air Showers and scattered/upward-coming muons. Particle deposited energy in the *WCD* identifies Electron/positron component, while scattered and backward muons are rejected using a pico-second *ToF* system.

## III. HODOSCOPE RESPONSE TO COSMIC RAY BACKGROUND

The response of the hodoscope bars refers to the signal produced in the *SiPM* photo-sensor when a charged particle

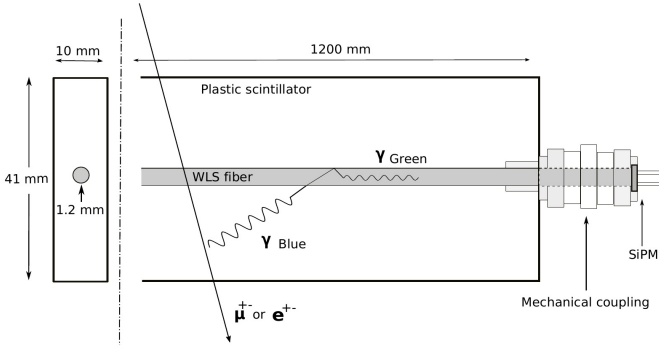


Fig. 2. This sketch represents the scintillator bar system, with an embedded WLS fiber placed in the center of the plastic scintillation bar and coupled to a SiPM. Charged particles crossing the bar produce scintillation photons in the blue-violet band. Those photons are absorbed and re-emitted in the WLS fiber as green photons. The fiber guides photons to the SiPM where they can produce a signal depending on their wavelength, as the SiPM spectral detection range is from 270 to 900 nm, with the maximum sensitivity around 450 nm).

crosses each scintillator bar. Indirect detection of secondary EAS photons is also possible mainly through Compton scattering and even pair creation. However, as the scintillation detector volume is relatively small, these mechanisms are highly improbable.

As shown in figure 2, charged particles impinging the scintillators produce photons in the blue-violet-ultra violet bands, which can be absorbed by the plastic material or collected by the WLS fiber. The fiber cladding helps to capture photons, conduct them through the fiber where they can be absorbed, re-emitted –in the green optical band– and guided to the photo-sensor device located at one of the extremes of the fiber[37].

In the following sections we shall discuss the *Geant4* [40] bar simulation model, the experimental setup to validate them (see section III B) and the estimation of the average response of the hodoscope panels to the passage of charged particles, especially in the Minimum Ionization Particle MIPs energy range.

#### A. The scintillator bar model

The *Geant4* geometric model of the bar consists of a parallelepiped of 4cm wide, 1cm high and 120cm long. We incorporate to this geometry a coating material –made of 15% of  $\text{TiO}_2$  and 85% of polystyrene– with a reflectivity of 1 and 0.25mm of thickness.

The scintillating bar is polystyrene, with an index of refraction,  $n = 1.50$ , and a photon absorption length of 5.5cm. There is a tunnel of 119.5cm long and 1.8mm of diameter, drilled through the central axis of the bar, where we place a multi-cladding WLS fiber. This looseness of 0.5cm at the end of the tunnel –filled with air to make the model as real as possible– avoids the escape of photons. The fiber 119.45cm-

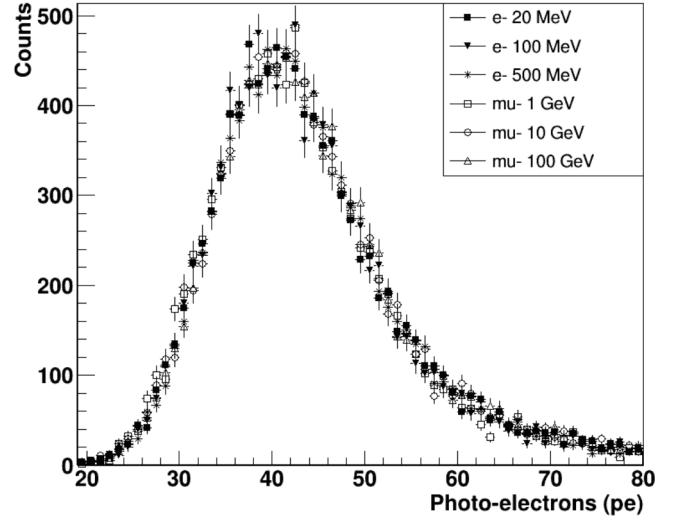


Fig. 3. Scintillator bar response to MIPs of different energy. As expected, both electrons and muons generate the same histogram profile, since the energy loss of all those particles is  $\sim 2.08\text{MeV}$ . This result validates the code used and therefore supports the veracity of the simulations of the scintillator bar. To obtain those histograms, we performed the interaction of 10000 particles (of each energy and type) with the bar. The average number of photo-electrons is around 40pe for all the particles, i.e., this detector is not able to distinguish muon events from noise.

tunnel 119.5cm configuration leaves a space of 0.05cm to locate the SiPM inside the tunnel.

A solid cylinder of poly-methyl methacrylate, with 119.45cm long and 0.5mm radius, models the fiber. The first clad of this fiber is a cylindrical shell of polyethylene, with an internal radius of 0.5mm and an external radius of 0.515mm. The second is a shell of fluorinated polyethylene, with an internal radius of 0.515mm and an external radius of 0.530mm. Both coatings have the same fiber length.

A square surface of a side of 1.3mm, attached to one of the fiber, represents the SiPMs. The simulations allow to set the SiPM photon detection efficiency, which depends on the wavelength of the photon hitting the SiPM, where the highest probability of Photo-Electrons (pe) generation is around 470nm [38].

Figure 3 displays the simulation results of the scintillator bar response to charged particles of different energy. The histogram of the number of photo-electrons generated by 10000 electrons of 20MeV, 100MeV and 500MeV has the same profile as those corresponding to the 10000 muons of 1GeV, 10GeV and 100GeV. This similarity occurs because those particles have the same stopping power in polystyrene, i.e.  $\frac{dE}{dx_{\text{pol}}} \approx 2\text{MeV cm}^2/\text{g}$  [41], so they all deposit about 2.08MeV of energy when passing through a centimeter of polystyrene. Therefore, our detector is not able to distinguish muons from electrons, and it is necessary to use the WCD to select the muon events from noise.

The mean value of those histograms is around 40pe, which is equivalent to 2.08MeV of energy deposited in the bar since those particles pass through vertically and the distance trav-

eled is 1 cm. The following simulations are for muons with 3GeV, which are the most frequent at the level of our observation point on the Cerro Machín volcano, thus, from now on, the *MIP* refers to this particular particle having this energy.

### 1. Attenuation of the photons in the Bar-Fiber-SiPM system

The light that propagates within the WLS fiber suffers an inevitable attenuation due to some photons escape from the optical guide, and others can be absorbed by the material while being transported to the *SiPM*. This attenuation depends on the length of the bar (which in this case is 120cm), so it is necessary to study how the attenuation behaves in our *Bar-Fiber-SiPM* system.

From the simulations of the scintillation detector, we can count the number of *pe* generated in the *SiPM* when a *MIP* crosses the bar at different distances  $x$ , where  $x$  is the distance between the point of impact and the location of the *SiPM*. These distances were chosen to take into account the width of the pixels of the hodoscope, i.e., 4cm wide; therefore  $x$  varies as,  $x = (2 + 4p)\text{cm}$   $p = 0, 1, 2, \dots, 29$ .

Figure 4 shows the result of this simulation. If the particle impacts at the position closest to *SiPM* (i.e.  $x = 2\text{cm}$ ), it has the maximum photo-electron intensity and, if it impacts farther away from the *SiPM*, the intensity decreases. A double exponential function  $F(x)$  fits the data and models this decrease

$$F(x) = 0.468e^{-0.003(2-x)} + 0.531e^{0.005(2-x)}. \quad (1)$$

From this plot, we have that the attenuation in the *Bar-Fiber-SiPM* system is around 7%, that agrees with the experimental results, around 11%[42], given by the figure 10.

The *MIP* detection with scintillator bar generates a number of *pe* in the *SiPM* at a time  $t$ . Now we want to estimate the time needed to collect the total number of photo-electrons produced. This total is about 40*pe* at  $x = 2\text{cm}$ , while at  $x = 118\text{cm}$  it is about 37*pe*. From the top of figure 5 it can be noticed that 40% of the total photo-electrons occurred in the first 10ns when the *MIP* has impacting the bar at 2cm of the *SiPM*. Observe from the bottom of the figure 5 –when the *MIP* has entered at 118cm of the *SiPM*–, that only 12% of the *pe* is produced in the same time. In both cases, the total number of *pe* is reached around 80ns, that is, the average time necessary to collect the total of *pe* produced by the passage of a muon, at any point of impact in the bar.

### 2. SiPM and fiber coupling

The *Geant4* model allows estimating how good is the coupling *SiPM*-fiber. We define the ideal *SiPM*-fiber when they are side by side, without any space between them. Thus, all the traveling photons at the edge of the fiber impact directly on the *SiPM*. As shown above, the obtained average number of photo-electrons, for an ideal coupling, is 40*pe*. A non-ideal coupling has space (filled with air) of 1.15mm between

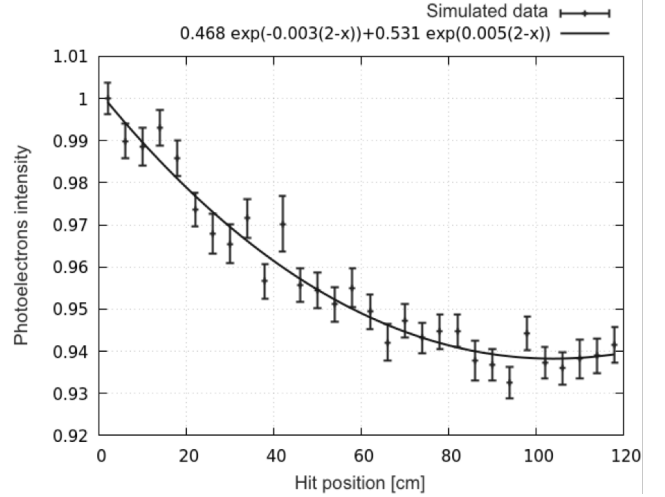


Fig. 4. The number of photo-electrons concerning the position of the impacting *MIP* in the bar. At  $x = 2\text{cm}$ , we have the maximum photo-electron intensity, and as the particle impacts farther away to the *SiPM*, the intensity decreases. A double exponential function fits the simulated data, and this behavior can be associated with the attenuation of the photons traveling through the fiber, that is around 7%

the *SiPM* and the fiber. The number of *pe* is reduced to 8, representing a loss of 80% of the signal compared to the ideal case, as shown in figure 6.

### B. Experimental results from the scintillator detector

As described before, the plastic scintillators of the *MuTe* panels allow the indirect detection of ionizing radiation from the offline analysis of the electrical signal produced in the *SiPMs*. Since the *SiPMs* have intrinsic noise, it is essential to know the detector to define a methodology to detect particles and correctly interpret the measured data. A first study guarantees that the *SiPM* are working in Geiger mode at any temperature. Section III B 1 presents the results of the dependence on the breakdown voltage with the temperature.

On the other hand, given that the scintillator, the fiber, and the *SiPM* are not 100% efficient, there are various parameters to take into account. For example, the material of the bars is opaque to photons with an average length of 5.5cm of attenuation. Then, to have a detector of 120cm length, a WLS fiber is placed inside the bar. The fibers guide the photons, but they can experiment attenuation despite being multi-layer, i.e., some photons can escape from the guide and even reflected in the border. This represents an additional problem when coupling different scintillators, and there will be edge effects related to the refractive index of each one. Therefore, with a controlled experiment, we must quantify the attenuation in these fibers and determine whether the coupling and the attenuation will be relevant in the case of the *MuTe* scintillator bars (see section III B 2).



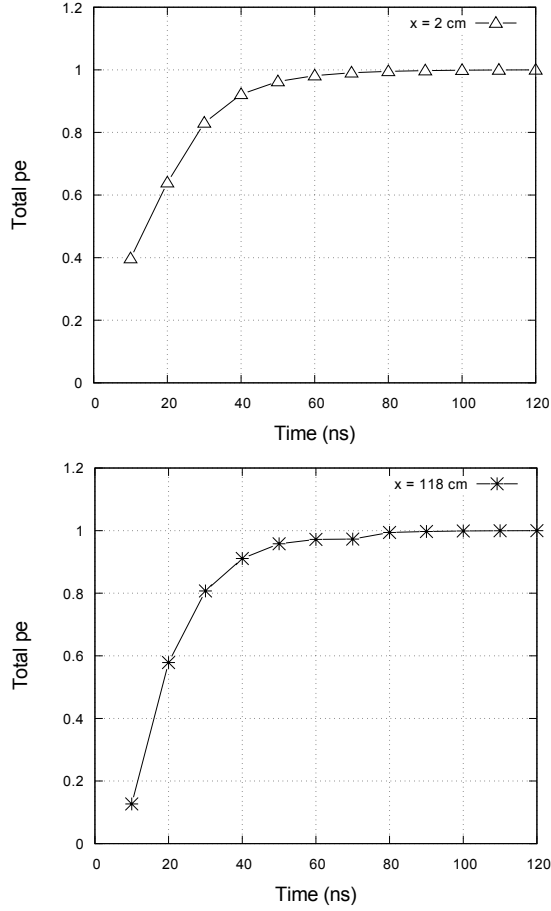


Fig. 5. Cumulative number of photo-electrons produced when a *MIP* hit the bar at 2cm from the *SiPM* (top) and at 118cm (bottom). It can be noticed that 40% of the Total *pe* occurred in the first 10ns when  $x = 2\text{cm}$  and when  $x = 118\text{cm}$ , only 12% of the *pe* is produced in the same time. In both cases, the total number of *pe* is reached around 80ns, that is, the average time necessary to collect the total of *pe* produced by the passage of a muon, at any point of impact in the bar.

### 1. Dependence of the breakdown voltage with the temperature

To study the response of each scintillator bar, we first studied the *SiPMs* thermal stability. *SiPMs* can change their mode of operation if the input voltage ( $V_{Bias}$ ) is less than the breakdown voltage ( $V_B$ ), and this parameter varies with temperature. Thus we need to find this functionality to guarantee that *SiPMs* always works in Geiger mode.

To establish this dependence, we build a temperature-controlled box regulated by a TEC1-12706 thermoelectric Peltier cell, mounted on an aluminum frame, where we place the *SiPM*. The control system consists of two sensors: one to vary the temperature and the other one to measure it on the *SiPM*. Figure 7 displays the results for the operation of this system for different target temperatures (10°C, 20°C, 40°C and 50°C). Note that the time required to reach the target temperature, in each case, is around  $(600 \pm 50)\text{s}$ .

Next, Dark-Current [43] measurements follow in the range

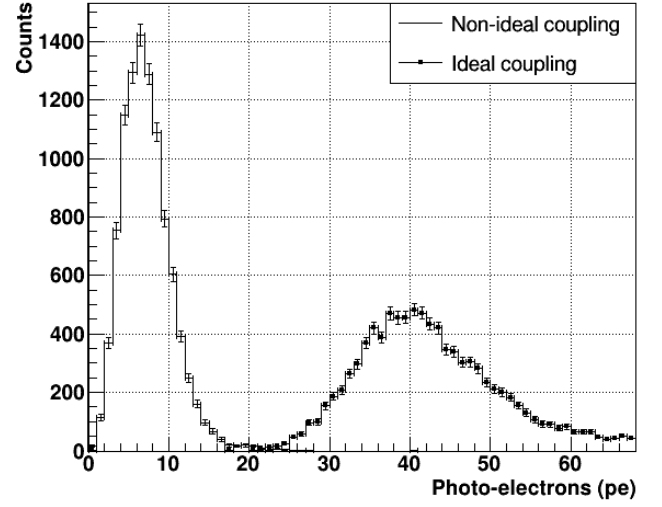


Fig. 6. Histogram of the number of *pe* resulting from the evaluation of the *SiPM* and fiber coupling. The squares curve represents the photo-electrons produced in the ideal case (when the *SiPM* and the fiber are side by side), while the simple line shows the non-ideal case, where the distance between the *SiPM* and the fiber is 1.15mm. The average number in the ideal case is around 40*pe* and in the non-ideal is around 8*pe*, i.e. the 80% of the signal is lost. This result gives an idea of when a bar-fiber-*SiPM* system of the real detector is badly coupled and should be replaced or verified.

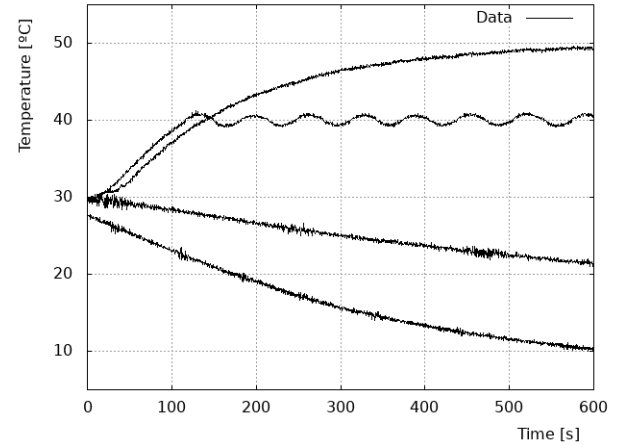


Fig. 7. Measurements of the system set-up time with different target temperatures: 10°C, 20°C, 40°C and 50°C. We can see that the time required to reach the target temperature in each case is around  $(600 \pm 50)\text{s}$ .

for 40V to 60V, for different temperatures and figure 8 illustrates the linear temperature dependence of  $V_B$ . It is clear that for each 10°C of temperature, the  $V_B$  changes around 0.45V.

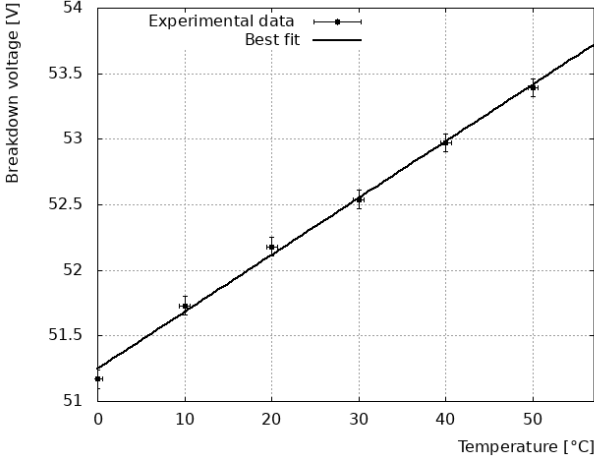


Fig. 8. Dependence of the breakdown voltage with the temperature for the *SiPM* Hamamatsu S13360-1350CS used in the MuTe hodoscope. It can be observed that the relation is linear, that is for every  $10^\circ\text{C}$  of temperature the  $V_B$  varies about  $0.45\text{V}$ .

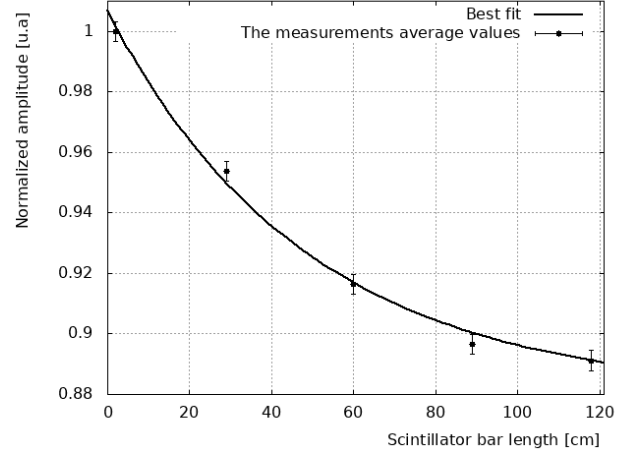


Fig. 10. Attenuation of the signal in the test bar obtained from the coincidence of three signals. The maximum amplitude is in the position closest to the *SiPM*, decreases by 11% at the opposite end.

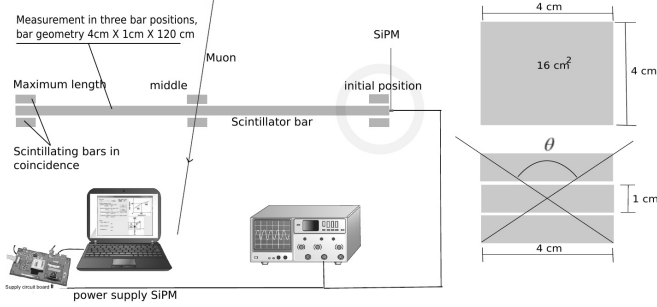


Fig. 9. Diagram of the experimental set-up to measure the bar signal attenuation. The three positions of interest are at both ends and the middle. An event is if there is a simultaneous signal in the three scintillators: the upper, the bar, and the lower one.

## 2. Attenuation measurements of the Bar-Fiber-SiPM system

To estimate the attenuation in the scintillator bars, we measure the signal produced by the passage of charged particles at both ends and the middle of the bar. Figure 9 illustrates the experimental set-up, which defines an event if there is a simultaneous signal in the three scintillators: the upper, the bar, and the lower one.

The trigger system, connected to a RedPitaya development card, records pulses with a frequency of 125 Mhz [44]. The system was synchronized to have pulses in coincidence, producing three input signals to the card and one output signal that corresponds to each position in the scintillator test bar. The coincidence system has an angle  $\theta$  for this configuration of  $106.26^\circ$ , as shown in Figure 9. The frequency of events per minute, measured with an oscilloscope, was  $10 \pm 1$  per minute for  $16\text{cm}^2$ . Thus, with this rate, it is possible to detect  $0.62 \text{ particles} \times \text{min} \times \text{cm}^2$ .

After a noise calibration, we record 10000 pulses in the three positions of interest. At the farthest end from the *SiPM*,

the fiber was cut to  $45^\circ$  to maximize photon leakage and to avoid secondary pulses by reflections at the end of the fiber.

From each average pulse, we calculate the mean deposited charge at the three positions. Then, we estimate the percentage of attenuation by normalizing and comparing the values, as shown in Figure 10. In our case, the difference between the mean charge value deposited at both ends is around 11%. An exponential function fits the attenuated signal as

$$H(x) = 0.880 + 0.126e^{(-0.02x)}. \quad (2)$$

## C. Simulated attenuation in the hodoscope

The probability of producing photo-electrons in the *SiPM* of horizontal and vertical bars is a crucial concept to determine the response of each panel of the hodoscope. The bar simulation generates the response of a detection panel to *MIPs*. Thus, independent events in a particular pixel  $P_{i,j}^F$  is given by

$$P_{i,j}^F = P_i^F \times P_j^F, \quad (3)$$

where  $P_i^F$  y  $P_j^F$  are the probabilities obtained in the horizontal bar  $i$  and in the vertical bar  $j$ , respectively.

Figure 11 displays the probability of photo-electrons produced by *MIPs* and hitting each panel pixel, obtained from equation 3.

These results are valid for both the front panel and the rear panel, and from figure 11, it clear that there is a difference between the zones. This difference around 12% can be associated with the attenuation of photons in the fiber, i.e., the pixels that are closer to the *SiPM* count more photo-electrons.

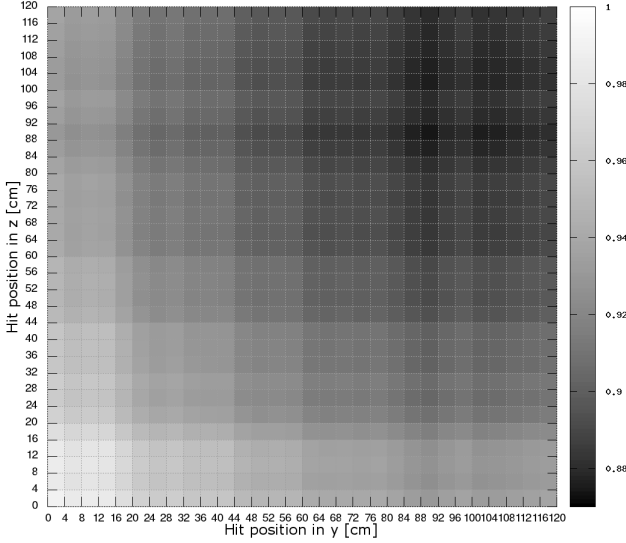


Fig. 11. The probability of photo-electron production in each pixel of a hodoscope panel by muons of 3 GeV of energy. Each frame represents a detection pixel and it can be seen that there is a difference between two zones of the panel. In the pixel  $P_{11}$ , where the SiPM of the horizontal bar and the vertical bar is only 2 cm from the point of impact of the muon, is produced the maximum number of  $pe$  while the  $pe$  decreases until 12% for pixels far from the SiPMs. This result is valid both for the front and the rear panel.

#### IV. THE WATER CERENKOV DETECTOR RESPONSE TO COSMIC BACKGROUND RADIATION

The WCD indirectly detects charged secondaries, by the Cerenkov photons generated by relativistic particles traveling through the contained water. The photo-multiplier tube counts photo-electrons according to its quantum efficiency, which depends on the wavelength of the impacting photon. In our case, the PMT Hamamatsu R5912 of the MuTe has a maximum detection probability value of 25% for photons with  $\lambda = 400$  nm [38]. The PMT located at the top of the metal container of purified water with 120 cm side, coated with a diffusive lining of Tyvek.

The following sections will discuss some results from the detector simulation, as well as the first data recorded by the WCD.

##### A. The WCD model

In *Geant4* the water container is a stainless steel cube of length  $l_c = 1.21$  m, with water inside water in a cube of  $l = 1.20$  m side. The water has a refractive index  $n$ , which varies between 1.3435 and 1.3608, and a photon absorption length ranging from 0.69 m to 2.90 m according to its energy. In the walls of the cube, the Tyvek is modeled as an optical

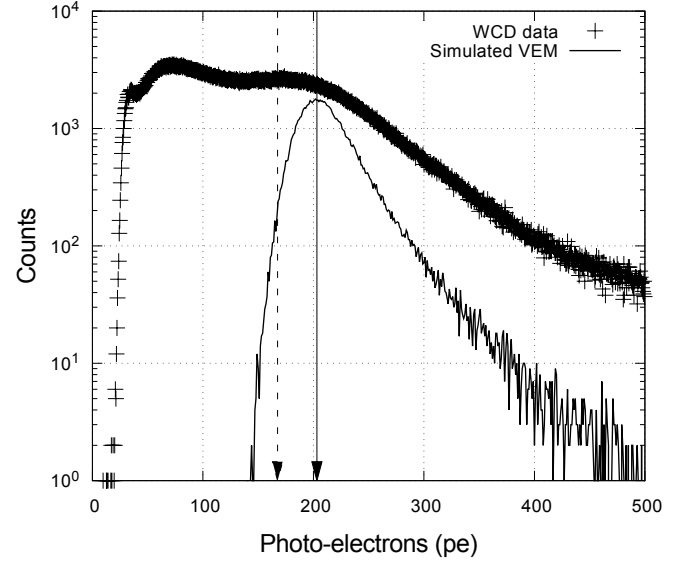


Fig. 12. Photo-electron histogram for one hour of data recorded by the WCD with a discrimination threshold of 110 mV. The histogram has two prominent humps, the electromagnetic at  $\sim 70$  pe and the muonic hump at  $\sim 167.5$  pe. The solid curve represents the simulated VEM histogram which mean value is  $\sim 203.2$  pe (solid arrow), for comparison with the measured value (dash arrow).

surface with a reflection index  $n_{\text{Tyvek}} = 1$ , which diffuses the Cerenkov photons.

For the PMT, the photo-cathode was simulated as an air half-ellipsoid with semiaxes  $s_x = 10.1$  cm,  $s_y = 10.1$  cm and  $s_z = 6.5$  cm, located on top of the water cube. The Quantum Efficiency (QE) of this device was introduced in the code, taking into account reference Hamamatsu R5912 [38]. The QE determines whether photons reaching the outer surface of the photo-cathode will be detected or not. These photons originate photo-electrons (denoted as  $pe$ ) by photoelectric effect. The WCD response is given in terms of  $pe$  generated by each particle interacting with it.

Notice that the inclusion of the QE of the PMT in the code, as a function dependent on  $\lambda$ , represents an improvement over the simulations of WCDs carried out previously within the research group. A unique efficiency of 25% is taken into account in [45], for the wavelength range between 330 nm and 570 nm. Therefore, the new code offers more precise results of the pulses produced by the passage of particles in water.

##### 1. Estimation of the Vertical Equivalent Muon unit

The Vertical Equivalent Muon (VEM) –defined as the average charge collected in the PMT when a high-energy muon vertically crosses the entire detector– is generally adopted as the unit to calibrate the energy deposited by incident particles and is independent of the detection position. Muons can be easily identified by installing plastic scintillators above and below the WCD [46].

*Geant4* code allows the injection of muons with a chosen

Table 1. Summary of the physical magnitudes obtained for the *VEM* and the *VE*: Length traveled in water ( $l$ ), Number of Cherenkov Photons produced ( $N$ ), Number of Photons that reach the *PMT* ( $N_{\text{PMT}}$ ), Number of Photoelectrons ( $N_{\text{FE}}$ ), Time of attenuation of the pulse ( $\tau$ ) and Length of attenuation ( $l_a$ ).

	$\mu^-$ (3 GeV)	$e^-$ (20 MeV)
$l$	$(120 \pm 1) \text{ cm}$	$(10 \pm 1) \text{ cm}$
$N$	$46857 \pm 13$	$3538 \pm 1$
$N_{\text{PMT}}$	$1617 \pm 1$	$132.1 \pm 0.1$
$N_{\text{pe}}$	$203.2 \pm 0.2$	$16.729 \pm 0.003$
$\tau$	$(42.12 \pm 0.01) \text{ ns}$	$(32.75 \pm 0.03) \text{ ns}$
$l_a$	$(7.332 \pm 0.001) \text{ m}$	$(9.430 \pm 0.002) \text{ m}$

energy and direction. We model injecting 100000 vertical muons with 3GeV in direction  $-\hat{z}$  towards the water, and the initial position given by the point  $P = (80, 80, 121) \text{ cm}$ , over the *WCD*. The portion of the number of Cherenkov photons,  $N$ , that reaches the external surface of the photo-cathode, is  $N_{\text{PMT}}$ .

The  $N_{\text{PMT}}$ , depending on its wavelength, produces a number of photo-electrons,  $N_{\text{pe}}$ . We have estimated the efficiency of the *WCD* with the following chain of events. One *VEM* of 3GeV generates around 46857 Cherenkov photons in 120cm. Next, only 1617 of those photons reach the external surface of the photo-cathode, and, due to its quantum efficiency, around an average 203.2 *pe* was produced. Thus, the system has a muon detection efficiency of 0.4%, that is,

$$\eta_{\text{WCD}} = \frac{N_{\text{FE}}}{N} 100\% = \frac{203.2}{46857} 100\% = 0.4\% \quad (4)$$

Figure 12 displays the comparison of the *VEM* simulated value ( $\sim 203.2 \text{ pe}$ ) with the measured  $\sim 167.5 \text{ pe}$ . This figure represents the *pe* histogram for one hour of data for a discrimination threshold of 110mV. The histogram has two prominent humps, the electromagnetic (electrons, positrons and gammas) hump at  $\sim 70 \text{ pe}$  and the muonic hump at  $\sim 167.5 \text{ pe}$  [18].

To compare the *WCD* response to muons and electrons at the Cerro Machín Volcano, we run simulations for 100000 vertical electrons, *VE*, of 20MeV at the same initial direction and point  $P$ . Figure 13 presents the corresponding histogram of the number of photo-electrons. The mean value of the *VE* is smaller than the *VEM*, around 16.7*pe* that represents a 8% of it.

Next, in the number of *pe* vs time displayed in plot 14 we sketch the *VEM* and *VE* pulses. From those histogram fits, we can obtain the attenuation time  $\tau$  and signal length  $l_a$ . Finally, the table IV A 1 summarize the comparison between both charged particles.

## 2. WCD response to the cosmic ray background radiation

The *LAGO ARTI* framework allows us to estimate of the *WCD* response to the cosmic ray background radiation flux ( $\Xi$ ) at any site [47]. This toolkit employs a *Geant4* code to estimate the number of Cerenkov photons detected by

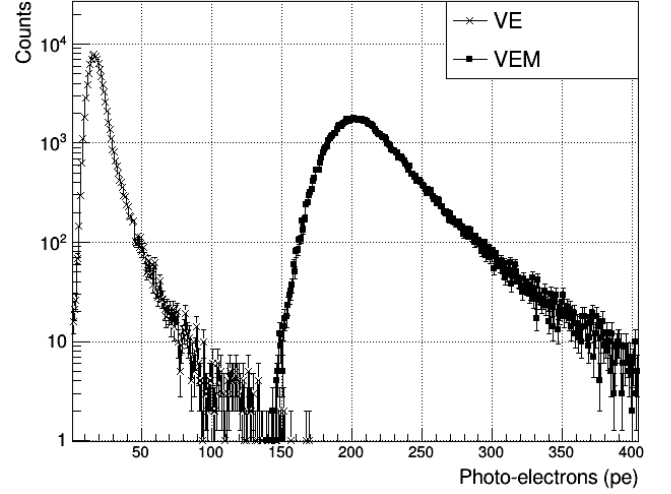


Fig. 13. Histogram of the number of photo-electrons produced due to the detection of vertical muons (squares) and vertical electrons (crosses) with the *WCD*. From the curve of the square, the mean value for the unit of calibration, *VEM*, is around 203.2*pe*. In comparison, the mean number produced by the *VE* is 16.7*pe*, that is the 8% of the *VE*. This result shows that the *WCD*

the *PMT* and employing its quantum efficiency. The *ARTI* framework uses the energy and the momentum of the particles from  $\Xi$  as input and obtains the flux by using the *CORSIKA* code [48], with a geomagnetic correction form *MAGCOS* code [49]. For other examples of the precise simulation chain see [50, 51].

Figure 15 plots the histogram of the number of photo-electrons, produced at Cerro Machín. The flux  $\Xi_{\text{CM}}$ ,

$$\Xi_{\text{CM}} = \frac{N_{\text{Sec}}}{7.5 \text{ s } 480 \text{ m}^2}, \quad (5)$$

is calculated over a circular area  $A = 480 \text{ m}^2$  placed 1cm above the detector, with a zenithal aperture of  $0 \leq \theta \leq 80^\circ$ , and where  $N_{\text{Sec}}$  = represents the number of secondaries at this particular site.

The different curves represent the contribution of various particles to the total response (empty circles). Note that this curve has two main peaks, the first one with a contribution of the electromagnetic component and the second one with the muonic component.

## V. CONCLUSIONS

As we have stated above, MuTe combines two detection techniques: a hodoscope with two detection planes of plastic scintillator bars, and a *WCD*, in an innovative setup which differentiates it from some previous detectors.

- **Scintillators panels:** Inspired by the experiences of other volcano muography experiments [52, 53], we



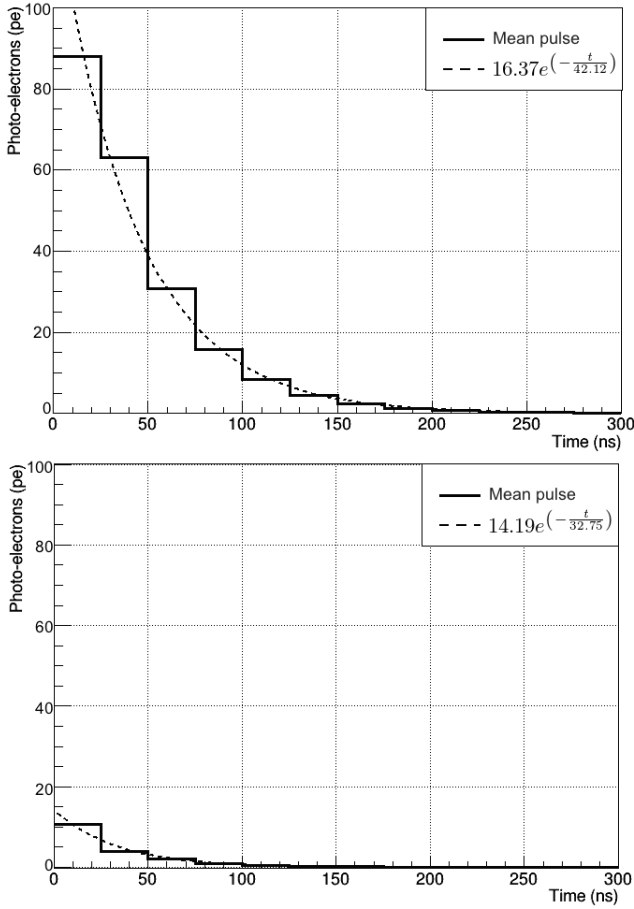


Fig. 14. Mean pulse corresponding to the *VEM* (top) and the *VE* (bottom) response. The dashed lines represent the best exponential fit of the pulses where the attenuation time  $\tau$  is around 42.12ns for the *VEM* and 32.75ns for the *VE*.

have designed two X-Y arrays of  $30 \times 30$  plastic scintillating strips ( $120\text{cm} \times 4\text{cm} \times 1\text{cm}$ ), made with Styron<sup>TM</sup> 665-W polystyrene doped with a mixture of liquid organic scintillators: 1% of 2,5-diphenyloxazole (PPO) and 0.03% of 1,4-bis (5-phenyloxazol-2-yl) benzene (POPOP). Each array has 900 pixels of  $4\text{ cm} \times 4\text{ cm} = 16\text{ cm}^2$ , which sums up  $14,400\text{ cm}^2$  of detection surface which can be separated up to  $D = 250\text{ cm}$ .

- **Water Cherenkov Detector:** The *WCD* is a purified water cube of  $120\text{ cm}$  side, located behind the rear scintillator panel, which acts as an absorbing element and as a third active coincidence detector. Due to its dimensions and location, it filters most of the background noise (low energies electrons, protons, and muons moving backward), which could cause overestimation in the hodoscope counts [34], and it is capable of isolating the muonic component of the incident particle flux. From the charge histogram, obtained by time integration of the individual pulses measured in the *WCD*, it is possible to separate two components of the incident flux: electromagnetic part (photon, electron & positron) and

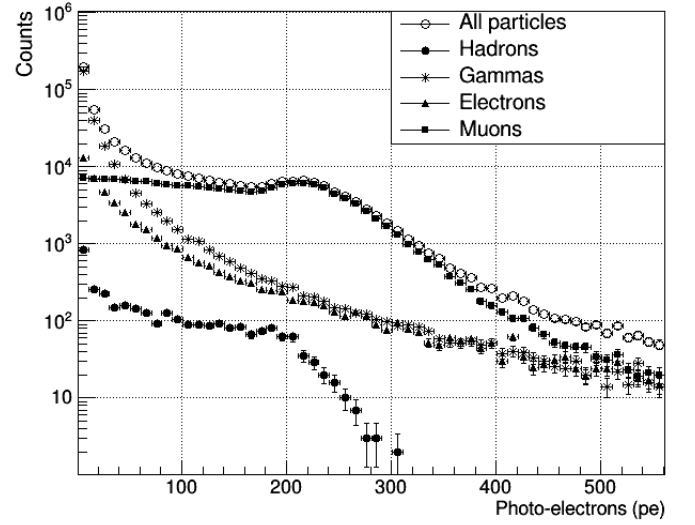


Fig. 15. Histogram of the number of photo-electrons produced by all particles detected in the *WCD*. The histogram has two prominent humps at  $\sim 5\text{pe}$  and at  $\sim 210\text{pe}$ . It can be noted that the first one is dominated for the electrons and gammas, i.e the electromagnetic component while the second one is dominated for the muons.

the  $\mu$ -component [50].

The Colombian *MuTe* combines particle identification techniques to discriminate noise background from data. It filters the primary noise sources for muography, i.e., the soft-component ( $e^\pm$ ) of *EAS* and scattered/upward-coming muons. Particle deposited energy identifies Electrons/positrons events in the *WCD*, while rejects scattered and backward muons using a pico-second Time-of-Flight system.

From the *Geant4* modeling of the scintillator detector, we obtain that the number of *pe* decreases around 7%, with respect to those produced at the end near of the *SiPM*. This reduction occurs due to the attenuation of the photons that travel in the fiber, since, the more distance they travel within it, the more energy they lose and lesser photons reach the *SiPMs*. This result is in agreement with the 11% attenuation obtained with the experimental setup described in section III B. This attenuation seems to be insignificant in the bar, but it is more noticeable in the hodoscope panels, since, the difference between the closest corner to the *SiPMs* and the furthest, is around 12%.

Regarding the *WCD* response, the value of simulated *VEM* and those recorded in the laboratory measurements, are in the same order of magnitude but present a percentage difference of 18% concerning the simulated value. This difference can be related by the various components of the electronics, where part of the signal can be lost.

From the results obtained, a muon detection trigger for the *MuTe* is proposed in terms of the energy deposited in each of its components. That is, the muon must deposit around  $2.08\text{MeV}$  in two scintillator bars on the front panel, then the same energy in two bars on the rear panel of the hodoscope,

to finally discriminate the signal from the noise in the WCD. Then, the muon must deposit around 240MeV of energy in the WCD to be counted as an event.

## ACKNOWLEDGMENTS

The authors acknowledge the financial support of Departamento Administrativo de Ciencia, Tecnología e Innovación of Colombia (ColCiencias) under contract FP44842-082-2015 and to the Programa de Cooperación Nivel II (PCB-II) MINCYT-CONICET-COLCIENCIAS 2015, under project CO/15/02. We are also very thankful to LAGO and

to the Pierre Auger Collaboration for their continuous support. The simulations in this work were partially possible thanks to The Red Iberoamericana de Computación de Altas Prestaciones (RICAP, 517RT0529), co-funded by the Programa Iberoamericano de Ciencia y Tecnología para el Desarrollo (CYTED) under its Thematic Networks Call. We also thank the computational support from the Universidad Industrial de Santander (SC3UIS) High Performance and Scientific Computing Centre. We would also like to thank Vicerrectoría Investigación y Extensión Universidad Industrial de Santander for its permanent sponsorship. We acknowledge very fruitful discussion with D. Sierra-Porta.

- 
- [1] J. Marteau, D. Gibert, N. Lesparre, F. Nicollin, P. Noli, and F. Giacoppo, *Nuclear Instruments and Methods in Physics Research Section A: Accelerators, Spectrometers, Detectors and Associated Equipment* **695**, 23 (2012), new Developments in Photodetection NDIP11.
- [2] R. Kaiser, *Philosophical Transactions of the Royal Society A: Mathematical, Physical and Engineering Sciences* **377**, 20180049 (2019).
- [3] G. Blanpied, S. Kumar, D. Dorroh, C. Morgan, I. Blanpied, M. Sossong, S. McKenney, and B. Nelson, *Nuclear Instruments and Methods in Physics Research Section A: Accelerators, Spectrometers, Detectors and Associated Equipment* **784**, 352 (2015).
- [4] K. Morishima, M. Kuno, A. Nishio, N. Kitagawa, Y. Manabe, M. Moto, F. Takasaki, H. Fujii, K. Satoh, and H. Kodama, *Nature* **552**, 386 (2017).
- [5] H. Gómez, C. Carloganu, D. Gibert, J. Jacquemier, Y. Karyotakis, J. Marteau, V. Niess, S. Katsanevas, and A. Tonazzo, in *Journal of Physics: Conference Series* (IOP Publishing, 2016) p. 052016.
- [6] H. Fujii, K. Hara, S. Hashimoto, F. Ito, H. Kakuno, S. Kim, M. Kochiyama, K. Nagamine, A. Suzuki, Y. Takada, Y. Takahashi, F. Takasaki, and S. Yamashita, *Progress of Theoretical and Experimental Physics* **2013** (2013), 10.1093/ptep/ptt046.
- [7] G. Saracino, L. Amato, F. Ambrosino, G. Antonucci, L. Bonechi, L. Cimmino, L. Consiglio, R. D. Alessandro, E. D. Luzio, G. Minin, P. Noli, L. Scognamiglio, P. Strolin, and A. Varriale, *Scientific Reports* **7** (2017), 10.1038/s41598-017-01277-3.
- [8] L. F. Thompson, J. P. Stowell, S. J. Fargher, C. A. Steer, K. L. Loughney, E. M. O'Sullivan, J. G. Gluyas, S. W. Blaney, and R. J. Pidcock, arXiv e-prints, arXiv:1906.05814 (2019), arXiv:1906.05814 [physics.ins-det].
- [9] H. K. M. Tanaka and L. Oláh, *Philosophical Transactions of the Royal Society A: Mathematical, Physical and Engineering Sciences* **377**, 20180143 (2019).
- [10] G. Cortés, *Informe de actividad volcánica segmento Norte de Colombia Diciembre de 2016*, Tech. Rep. (Reporte interno, Manizales, Colombia. INGEOMINAS, 2016).
- [11] A. Agudelo, *Informe técnico de actividad de los volcanes Nevado del Huila, Puracé y Sotará, durante el periodo de Diciembre de 2016*, Tech. Rep. (Reporte Interno, Popayan, Colombia, Servicio Geológico Colombiano, 2016).
- [12] E. Muñoz, *Informe mensual de actividad de los volcanes Galeras, Cumbal, Chiles y Cerro Negro, Las Ánimas, Dona Juana y Azufral*, Tech. Rep. (Reporte interno, Pasto, Colombia. INGEOMINAS, 2017).
- [13] H. Asorey, L. A. Núñez, J. D. Sanabria-Gómez, C. Sarmiento-Cano, D. Sierra-Porta, M. Suarez-Duran, M. Valencia-Otero, and A. Vesga-Ramírez, ArXiv e-prints (2017), arXiv:1705.09884 [physics.geo-ph].
- [14] H. Asorey, R. Calderón-Ardila, C. R. Carvajal-Bohorquez, S. Hernández-Barajas, L. Martínez-Ramírez, A. Jaimes-Motta, F. León-Carreño, J. Peña-Rodríguez, J. Pisco-Guavabe, J. Sanabria-Gómez, M. Suárez-Durán, A. Vásquez-Ramírez, K. Forero-Gutiérrez, J. Salamanca-Coy, L. A. Núñez, and D. Sierra-Porta, *Scientia et Technica* **23**, 391 (2018).
- [15] H. Asorey, R. Calderón-Ardila, K. Forero-Gutiérrez, L. A. Núñez, J. Peña-Rodríguez, J. Salamanca-Coy, J. Sanabria-Gómez, J. Sánchez-Villafrales, and D. Sierra-Porta, *Scientia et Technica* **23**, 386 (2018).
- [16] I. Guerrero, D. Cabrera, J. Paz, J. Estrada, C. Villota, E. Velasco, F. Fajardo, O. Rodriguez, J. Rodriguez, D. Arturo, D. Dueñas, D. Torres, J. Ramirez, J. Revelo, G. Ortega, D. Benavides, J. Betancourt, A. Tapia, and D. Martínez-Caicedo, in *Journal of Physics: Conference Series* (IOP Publishing, 2019) p. 012020.
- [17] J. Useche-Parra and C. Avila-Bernal, *Journal of Instrumentation* **14**, P02015 (2019).
- [18] J. Peña-Rodríguez, A. Vásquez-Ramírez, J. Sanabria-Gómez, L. Núñez, D. Sierra-Porta, and H. Asorey, in *36th International Cosmic Ray Conference (ICRC2019)*, Vol. 36 (2019).
- [19] A. Anastasio, F. Ambrosino, D. Basta, L. Bonechi, M. Brianzi, A. Bross, S. Callier, A. Caputo, R. Ciaranfi, L. Cimmino, R. D'Alessandro, L. D'Auria, C. de La Taille, S. Energico, F. Garufi, F. Giudicepietro, A. Lauria, G. Macedonio, M. Martini, V. Masone, C. Mattone, M. Montesi, P. Noli, M. Orazi, G. Passeggio, R. Peluso, A. Pla-Dalmau, L. Raux, P. Rubinov, G. Saracino, E. Scarlini, G. Scarpato, G. Sekhniaidze, O. Starodubtsev, P. Strolin, A. Taketa, H. Tanaka, and A. Vanzanella, *Nuclear Instruments and Methods in Physics Research Section A: Accelerators, Spectrometers, Detectors and Associated Equipment* **732**, 423 (2013), vienna Conference on Instrumentation 2013.
- [20] C. Carloganu, V. Niess, S. Bene, E. Busato, P. Dupieux, F. Fehr, P. Gay, D. Miallier, B. Vulpescu, and P. Boivin, *Geoscientific Instrumentation, Methods and Data Systems* **2**, 55 (2013).
- [21] N. Lesparre, D. Gibert, J. Marteau, Y. Déclais, D. Carbone, and E. Galichet, *Geophysical Journal International* **183**, 1348 (2010).

- [22] K. Nagamine, Proceedings of the Japan Academy, Series B **92**, 265 (2016).
- [23] R. Sehgal, V. Kashyap, I. Kanungo, A. Saxena, A. Jain, A. Jindal, V. Singh, P. Kanavi, S. Sehgal, and G. Kekre, in *DAE Symp. Nucl. Phys.*, Vol. 61 (2016) pp. 1034–1035.
- [24] F. Fehr and T. Collaboration, in *Journal of Physics: Conference Series* (IOP Publishing, 2012) p. 052019.
- [25] S. Bouteille, D. Attié, P. Baron, D. Calvet, P. Magnier, I. Mandjavidze, M. Riallot, and M. Winkler, Nuclear Instruments and Methods in Physics Research Section A: Accelerators, Spectrometers, Detectors and Associated Equipment **834**, 223 (2016).
- [26] L. Oláh, H. Tanaka, T. Ohminato, and D. Varga, Scientific reports **8**, 3207 (2018).
- [27] N. Lesparre, J. Marteau, Y. Déclais, D. Gibert, B. Carlus, F. Nicollin, and B. Kergosien, *Geoscientific Instrumentation Methods and Data Systems* **1**, 33 (2012).
- [28] H. Tanaka, T. Uchida, M. Tanaka, H. Shinohara, and H. Taira, *Geophysical Research Letters* **36** (2009), 10.1029/2008GL036451.
- [29] K. Nagamine, M. Iwasaki, K. Shimomura, and K. Ishida, *Nuclear Instruments and Methods in Physics Research Section A: Accelerators, Spectrometers, Detectors and Associated Equipment* **356**, 585 (1995).
- [30] P. Aguiar, E. Casarejos, J. Silva-Rodríguez, J. Vilan, and A. Iglesias, IEEE Transactions on Nuclear Science **62**, 1233 (2015).
- [31] S. Tang, Y. Yu, Y. Zhou, Z. Sun, X. Zhang, S. Wang, K. Yue, L. Liu, F. Fang, and D. Yan, Chinese Physics C **40**, 056001 (2016).
- [32] R. Nishiyama, S. Miyamoto, and N. Naganawa, *Geoscientific Instrumentation, Methods and Data Systems* **3**, 29 (2014).
- [33] T. Kusagaya and H. Tanaka, Proceedings of the Japan Academy, Series B **91**, 501 (2015).
- [34] R. Nishiyama, A. Taketa, S. Miyamoto, and K. Kasahara, *Geophysical Journal International* **206**, 1039 (2016).
- [35] H. Gómez, D. Gibert, C. Goy, K. Jourde, Y. Karyotakis, S. Katsanevas, J. Marteau, M. Rosas-Carbajal, and A. Tonazzo, *Journal of Instrumentation* **12**, P12018 (2017).
- [36] A. Pla-Dalmau, A. D. Bross, and V. V. Rykalin, in *2003 IEEE Nuclear Science Symposium. Conference Record (IEEE Cat. No. 03CH37515)*, Vol. 1 (IEEE, 2003) pp. 102–104.
- [37] *Plastic Scintillating Fibers*, Saint-Gobain Ceramics & Plastics (2017), rev. 1.
- [38] *MPPCs for precision measurement*, Hamamatsu (2018), rev. 1.
- [39] A. Filevich, P. Bauleo, H. Bianchi, J. R. Martino, and G. Torlasco, Nuclear Instruments and Methods in Physics Research Section A: Accelerators, Spectrometers, Detectors and Associated Equipment **423**, 108 (1999).
- [40] S. Agostinelli, J. Allison, K. Amako, J. Apostolakis, H. Araujo, P. Arce, M. Asai, D. Axen, S. Banerjee, G. Barrand, F. Behner, L. Bellagamba, J. Boudreau, L. Broglia, A. Brunengo, H. Burkhardt, S. Chauvie, J. Chuma, R. Chytrcek, G. Cooperman, G. Cosmo, P. Degtyarenko, A. Dell’Acqua, G. Depaola, D. Dietrich, R. Enami, A. Feliciello, C. Ferguson, H. Fesefeldt, G. Folger, F. Foppiano, A. Forti, S. Garelli, S. Giani, R. Giannitrapani, D. Gibin, J. G. Cadenas, I. González, G. G. Abril, G. Greeniaus, W. Greiner, V. Grichine, A. Grossheim, S. Guatelli, P. Gumplinger, R. Hamatsu, K. Hashimoto, H. Hasei, A. Heikkinen, A. Howard, V. Ivanchenko, A. Johnson, F. Jones, J. Kallenbach, N. Kanaya, M. Kawabata, Y. Kawabata, M. Kawaguti, S. Kelner, P. Kent, A. Kimura, T. Kodama, R. Kokoulin, M. Kossov, H. Kurashige, E. Lamanna, T. Lampén, V. Lara, V. Lefebvre, F. Lei, M. Liendl, W. Lockman, F. Longo, S. Magni, M. Maire, E. Medernach, K. Minamimoto, P. M. de Freitas, Y. Morita, K. Murakami, M. Nagamatsu, R. Nartallo, P. Nieminen, T. Nishimura, K. Ohtsubo, M. Okamura, S. O’Neale, Y. Oohata, K. Paech, J. Perl, A. Pfeiffer, M. Pia, F. Ranjard, A. Rybin, S. Sadilov, E. D. Salvo, G. Santin, T. Sasaki, N. Savvas, Y. Sawada, S. Scherer, S. Sei, V. Sirotenko, D. Smith, N. Starkov, H. Stoecker, J. Sulkimo, M. Takahata, S. Tanaka, E. Tcherniaev, E. S. Tehrani, M. Tropeano, P. Truscott, H. Uno, L. Urban, P. Urban, M. Verderi, A. Walkden, W. Wander, H. Weber, J. Wellisch, T. Wenaus, D. Williams, D. Wright, T. Yamada, H. Yoshida, and D. Zschiesche, Nuclear instruments and methods in physics research section A: Accelerators, Spectrometers, Detectors and Associated Equipment **506**, 250 (2003).
- [41] D. Michael, P. Adamson, T. Alexopoulos, W. Allison, G. Alner, K. Anderson, C. Andreopoulos, M. Andrews, R. Andrews, C. Arroyo, *et al.*, Nuclear Instruments and Methods in Physics Research Section A: Accelerators, Spectrometers, Detectors and Associated Equipment **596**, 190 (2008).
- [42] R. Calderón-Ardila, *Estudio de Centelladores Plásticos en el Proyecto MuTe para Muografía de Volcanes*, Master thesis in geophysics, School of Physics, Universidad Industrial de Santander, Bucaramanga, Colombia (2019).
- [43] D. Renker, Nuclear Instruments and Methods in Physics Research Section A: Accelerators, Spectrometers, Detectors and Associated Equipment **567**, 48 (2006).
- [44] R. Pitaya, Release 0.97. url: [\(http://redpitaya.readthedocs.io/en/latest/\(visited on 02/11/2017\)\)](http://redpitaya.readthedocs.io/en/latest/(visited on 02/11/2017)) (2016).
- [45] R. Calderón, H. Asorey, and L. Núñez, Nuclear and Particle Physics Proceedings **267**, 424 (2015).
- [46] A. Etchegoyen, P. Bauleo, X. Bertou, C. Bonifazi, A. Filevich, M. Medina, D. Melo, A. Rovero, A. Supanitsky, and A. Tamashiro, *Nuclear Instruments and Methods in Physics Research Section A: Accelerators, Spectrometers, Detectors and Associated Equipment* **545**, 602 (2005).
- [47] C. Sarmiento-cano, M. Suárez-Durán, A. Vázquez-Ramírez, A. Jaimes-Motta, R. Calderón-Ardila, and J. Peña-Rodríguez, in *36th International Cosmic Ray Conference (ICRC2019)*, Vol. 36 (2019).
- [48] D. Heck, J. Knapp, J. Capdevielle, G. Schatz, and T. Thouw, *CORSIKA : A Monte Carlo Code to Simulate Extensive Air Showers*, Tech. Rep. FZKA 6019 (Forschungszentrum Karlsruhe GmbH, 1998).
- [49] L. Desorgher, *MAGNETOSCOSMICS, Geant4 application for simulating the propagation of cosmic rays through the Earth magnetosphere*, Tech. Rep. (Physikalisches Institut, University of Bern, Bern, Germany, 2003).
- [50] H. Asorey, S. Dasso, L. Núñez, Y. Pérez, C. Sarmiento-Cano, M. Suárez-Durán, and the LAGO Collaboration, in *The 34th International Cosmic Ray Conference*, Vol. PoS(ICRC2015) (2015) p. 142.
- [51] H. Asorey, L. A. Núñez, and M. Suárez-Durán, Space Weather **16**, 461 (2018).
- [52] T. Uchida, H. K. Tanaka, and M. Tanaka, IEEE Transactions on Nuclear Science **56**, 448 (2009).
- [53] D. Gibert, F. Beauducel, Y. Déclais, N. Lesparre, J. Marteau, F. Nicollin, and A. Tarantola, Earth, planets and space **62**, 153 (2010).